

Electronic supplementary information

Coherent illumination for lens-free time-lapse imaging of living cells

Considering the virtue of lensless imaging solutions, many research efforts have been made in this direction, resulting in excellent light emitting diode (LED)-based systems. The basic lens-free LED platform, developed by Ozcan et al.^{1,2}, is similar to our set-up in Fig. 1A but with a LED light source in combination with a pinhole (~50 to 150 μm) to improve the spatial coherence of the LED light. In this way partially coherent digital in-line holography is achieved. Due to the low coherence length of this illumination type, the sample and image sensor are required to be very close together, and the resulting spatial resolution is larger than the pixel pitch of the imaging chip. Next to cell identification^{3,4} and semen analysis⁵, this method was used to monitor adhering and dividing cells^{6,7} and random motility of fibroblasts on polyacrylamide gels⁸. This could be achieved as these cells are substantially larger than the pixel pitch of the systems, however the fine morphology (3-5 μm) of the individual cells could not be resolved.

Resolution of the partially coherent LED-based systems can be improved by making use of the principle of a synthetic aperture. With this technique, sub-pixel resolution is obtained by numerically re-combining a large set of low-resolution holograms of the sample. The most common way to obtain this low-resolution hologram set is by shifting the object or light source over sub-pixel distances, known as the pixel super-resolution technique⁹. Using this technique, morphology of individual sperm and red blood cells could be resolved¹⁰. However, in order to obtain these results, a large number of sub-pixel shifted holograms needed to be recorded: 36 and even up to 100 holograms. Another way in which the set of shifted low-resolution holograms can be obtained is through holographic optofluidic microscopy, i.e. flowing the sample through a microfluidic channel and imaging the same object multiple times¹¹⁻¹³. Detailed pictures of *C. Elegans*, unicellular parasites, and pollen can be obtained in this way^{14,15}. Finally, resolution can be improved and even 3D reconstructions obtained with lens-free diffractive tomography, in which a low-resolution hologram set is obtained by rotating the light source. In this way 3D morphology of a prostatic cell network grown in Matrigel could be elucidated¹⁶. However, this also requires multiple light sources, a large set of recorded holograms, and a substantial amount of computational power.

In these systems, compromises were made in order to achieve sub-micron resolution using synthetic aperture and partially coherent LED illumination. First, acquisition speed is very low as a large number (36-100) of holograms need to be recorded in order to reconstruct one high-resolution image of the sample¹⁰. Second, accurate control over the movement of the sample or light source is needed in order to perform the sub-pixel shifts, and extremely precise and expensive motorized stages are necessary for this. This could be avoided using an array of LEDs that are spaced at specific and accurate distances¹⁷, however, this complicates and enlarges the set-up design. Recent reports show that for this purpose low-cost axial translation stages can be used if combined with specialized rotational field transformation software that compensates for tilt changes in holograms recorded at different heights⁹. Third, the complexity of the advanced algorithms needed to compute sub-pixel resolution is greatly increased, resulting in huge memory requirements and very long calculation times¹⁸, and a direct/live view of the sample that is being examined is impossible.

In order to simplify the image acquisition and reconstruction process, lasers can be used as a high-coherent light source. Lasers are commonly used for digital in-line holography, but many use an objective for focusing of the light into the pinhole and thus cannot be considered as truly lens-free¹⁹⁻²³. As both the temporal and spatial coherence of lasers is much higher than that of LEDs, a single recorded hologram will contain more information. This implies that for high-coherent light sources the obtained resolution of reconstructed images using only few input holograms and hence less complex algorithms is higher than a similar setup with LEDs. In this way image recording and reconstruction times are substantially decreased, enabling live views of the imaged sample²⁴. Next to this, the set-up design remains simple, as small and inexpensive semiconductor laser diodes are used and sub-pixel shifting or light source tilting is avoided. The presented LFI system uses four pigtailed laser diodes that are all coupled into one single mode optical fiber, avoiding alignment issues. The lasers are kept outside of the cell culture incubator and the light is guided into the incubator by the fiber to illuminate the sample and image sensor.

Although high-coherent laser light sources yield high quality holograms, they do introduce extra background signal. Speckle noise and multiple-reflection interference effects, generating extra background, are specific for laser illumination. Speckle noise was minimized by stabilizing the lasers through accurate temperature and power control. Next to this, the single mode optical fiber that is used to guide the light also serves as a spatial filter, severely reducing speckle noise. However, some speckle can still be observed in the LFI pictures obtained by our setup (Fig. S7A). Considering that the obtained picture quality is sufficient for the application at hand, no further action was taken to remove the remaining speckle noise using post-processing algorithms. Another issue with laser illumination is that due to the high spatial coherence, interference occurs over larger distances. This means that the light diffracted by different cells, or cells and other structures in the sample, also adds to the complete interference pattern that is measured at the detector. In comparison, due to the small coherence length of partially coherent LED light, interference only occurs on small length scales, meaning that signals from different cells do not interfere with each other and are only

superposed in the recorded hologram. This multi-interference issue is most relevant when cell motility in microchannels is imaged. Edge artefacts, e.g., dark areas and ring-like patterns, can be observed at the edges of the microchannels, and the repetitive pattern of channels causes shadow lines in between two consecutive channels (Fig. S7B). As a result, cells located close to the edges of the channels can be partially blurred (Fig. S7C). Care needs to be taken when micropatterns are designed (e.g., microchannel spacing should be optimized so that interference patterns do not interfere with signal coming from the cells) so as not to obscure the cells. The microstructures in this paper consisted of microchannels with widths of 6 μm spaced by 50 μm . Although edge artifacts could obscure cells at the edges of the microchannels, cell tracking was only performed on cells that are located completely inside the microchannels, for which interference noise was minimal and fine morphology could be resolved.

With digital in-line holography, the information that can be obtained suffers from the well-known inherent twin-image problem. In the reconstruction process there will always be two images present, i.e. the original object at the wanted focal plane and its conjugate around the origin. This out-of-focus twin image of the reconstructed object will cause blurring and will reduce image quality²⁵. Many possible solutions to this problem have been published^{26,27}. In our work an iterative phase retrieval technique is used based on 4 input holograms recorded using laser illumination at 4 different wavelengths²⁴. This is a very elegant solution, as only 4 holograms need to be recorded, resulting in short image acquisition times (~6 ms). Also, thanks to the fiber-optics approach used, neither the sample nor the light source needs to be moved or rotated, as the 4 different lasers are all coupled into the same optical fiber, resulting in an extremely robust system that minimizes misalignment between the different holograms. It is very important to avoid misalignment, as this can cause problems in convergence of the iterative phase retrieval algorithm. Misalignment is a source of noise that can accumulate due to the iterative algorithm and lead to total degradation of the reconstructed image. Although there are risks related to the use of an iterative approach, i.e. convergence issues and local solutions²⁸, these do not play a role in our approach as total convergence was not aspired. Only 10 to 50 iterations were executed, of which the first few iterations provide the greatest quality improvements. This software does not need the calculation power and memory capacities of expensive computer servers, and due to the very limited amount of iterations computing times are very short, delivering single-cell resolution reconstructed images in less than 1 minute.

Although imaging of cells with multiple lens-free systems has been reported, it has rarely been used for live-cell imaging. In fact, Pushkarsky et al.⁸ and Kesavan et al.^{6,7} are the first to report on the use of lens-free systems in the standard cell culture environment. In both cases, a set-up using LED illumination in combination with a pinhole was placed in the incubator, and cells were imaged over periods ranging from few hours to few days. The field of view was ~24 mm², however resolution was limited, i.e. fine lamellipodial and filopodial extensions (3–5 μm) could not be resolved. Cell adhesion, proliferation, and motility parameters were successfully deduced from these time-lapse imaging experiments, but single cell morphology was not resolved. Application of the synthetic aperture techniques for the live-cell imaging purpose to obtain sub-micron resolution is problematic, as it is important that the imaging speed is faster than that of the biological processes, hence there is not enough time to record a set of 100 holograms without any cell movement. The LFI set-up presented in this work is ideally suited for live-cell imaging purposes as it combines short acquisition times (6 ms), large field of view (29 mm²), and good resolution (1.2 μm). High imaging speeds can be combined with fine resolution as a result of the high-coherent laser illumination that enables high resolution hologram recording.

Supplementary references

1. A. Ozcan and U. Demirci, *Lab on a chip*, 2008, **8**, 98-106.
2. O. Mudanyali, D. Tseng, C. Oh, S.O. Isikman, I. Sencan, W. Bishara, C. Oztoprak, S. Seo, B. Khademhosseini and A. Ozcan, *Lab on a Chip*, 2010, **10**, 1417-1428.
3. T. W. Su, S. Seo, A. Erlinger and A. Ozcan, *Biotechnology and bioengineering*, 2009, **102**, 856-868.
4. S. Seo, T. W. Su, D. K. Tseng, A. Erlinger and A. Ozcan, *Lab on a chip*, 2009, **9**, 777-787.
5. T. W. Su, A. Erlinger, D. Tseng and A. Ozcan, *Analytical chemistry*, 2010, **82**, 8307-8312.
6. S. V. Kesavan, F. P. Navarro, M. Menneteau, F. Mittler, B. David-Watine, N. Dubrulle, S. L. Shorte, B. Chalmond, J. M. Dinten and C. P. Allier, *Journal of biomedical optics*, 2014, **19**, 36004.
7. S. V. Kesavan, F. Momey, O. Cioni, B. David-Watine, N. Dubrulle, S. Shorte, E. Sulpice, D. Freida, B. Chalmond, J. M. Dinten, X. Gidrol and C. Allier, *Scientific reports*, 2014, **4**, 5942.
8. I. Pushkarsky, Y. Lyb, W. Weaver, T. W. Su, O. Mudanyali, A. Ozcan and D. Di Carlo, *Scientific reports*, 2014, **4**, 4717.
9. A. Greenbaum, Y. Zhang, A. Feizi, P. L. Chung, W. Luo, S. R. Kandukuri and A. Ozcan, *Science Translational Medicine*, 2014, **6**, 267ra175.
10. A. Greenbaum, W. Luo, T.-W. Su, Z. Göröcs, L. Xue, S. O. Isikman, A. F. Coskun, O. Mudanyali and A. Ozcan, *Nature Methods*, 2012, **9**, 889-895.
11. G. Zhen, S.A. Lee, S. Yang and C. Yang, *Lab on a Chip*, 2010, **10**, 3125-3129.
12. J. Wu, G. Zheng, L.M. Lee, *Lab on a Chip*, 2012, **12**, 3566-3575.
13. V. Bianco, M. Paturzo, V. Marchesano, I. Gallotta E. Di Schiavi and P. Ferraro, *Lab on a Chip*, 2015, **15**, 2117-2124.

14. S.O. Isikman, W. Bishara, H. Zhu and A. Ozcan, *Proceedings of Annual International Conference of the IEEE Engineering in Medicine and Biology Society*, 2011, **2011**, 8463-8466.
15. W. Bishara, H. Zhu and A. Ozcan, *Optics Express*, 2010, **18**, 27499-27510.
16. F. Momey, A. Berdeu, T. Bordy, J.-M. Dinten, F. K. Marcel, N. Picollet-D'hahan, X. Gidrol and C. Allier, *Biomedical Optics Express*, 2016, **7**, 949-962.
17. A. Greenbaum, N. Akbari, A. Feizi, W. Luo and A. Ozcan, *PLoS One*, 2013, **8**, e76475.
18. S. O. Isikman , A. Greenbaum , W. Luo , A. F. Coskun and A. Ozcan, *PLoS One*, 2012, **7**, e45044.
19. D. Vercruysee, A. Dusa, R. Stahl, G. Vanmeerbeeck, K. de Wijs, C. Liu, D. Prodanov, P. Peumans and L. Lagae, *Lab on a chip*, 2015, **15**, 1123-1132.
20. J. Garcia-Sucerquia, W. Xu, S. K. Jericho, P. Klages, M. H. Jericho and H. J. Kreuzer, *Applied optics*, 2006, **45**, 836-850.
21. W. Xu, M. H. Jericho, I. A. Meinertzhagen and H. J. Kreuzer, *Proceedings of the National Academy of Sciences of the United States of America*, 2001, **98**, 11301-11305.
22. V. Mico and Z. Zalevsky, *Journal of biomedical optics*, 2010, **15**, 046027.
23. F. Merola, P. Memmolo, L. Miccio, V. Bianco, M. Paturzo and P. Ferraro, *Proceedings of the Institute of Electrical and Electronics Engineers*, 2015, **203**, 192-204.
24. R. Stahl, G. Vanmeerbeeck, G. Lafruit, R. Huys, V. Reumers, A. Lambrechts, C.-K. Liao, C.-C. Hsiao, M. Yashiro, M. Takemoto, T. Nagata, S. Gomi, K. Hatabayashi, Y. Oshima, S. Ozaki, N. Nishishita and S. Kawamata, *The International Society for Optics and Photonics Proceedings*, 2014, **8947**, doi: 10.1117/12.2037619.
25. M. Guizar-Sicairos and J. R. Fienup, *Journal of the Optical Society of America A*, 2012, **29**, 2367-2375.
26. B.M. Hennelly, D.P. Kelly, N. Pandey and D.S. Monaghan, *Proceedings of the China-Ireland Information and Communications Technologies conference*, 2009, 241-245.
27. E. Stoykova, H. Kang, J. Park, *Chinese Optics Letters*, 2014, **12**, 060013.
28. J.R. Fienup, *Applied Optics*, 1982, **21**, 2758-2769.

Supplementary figure legends

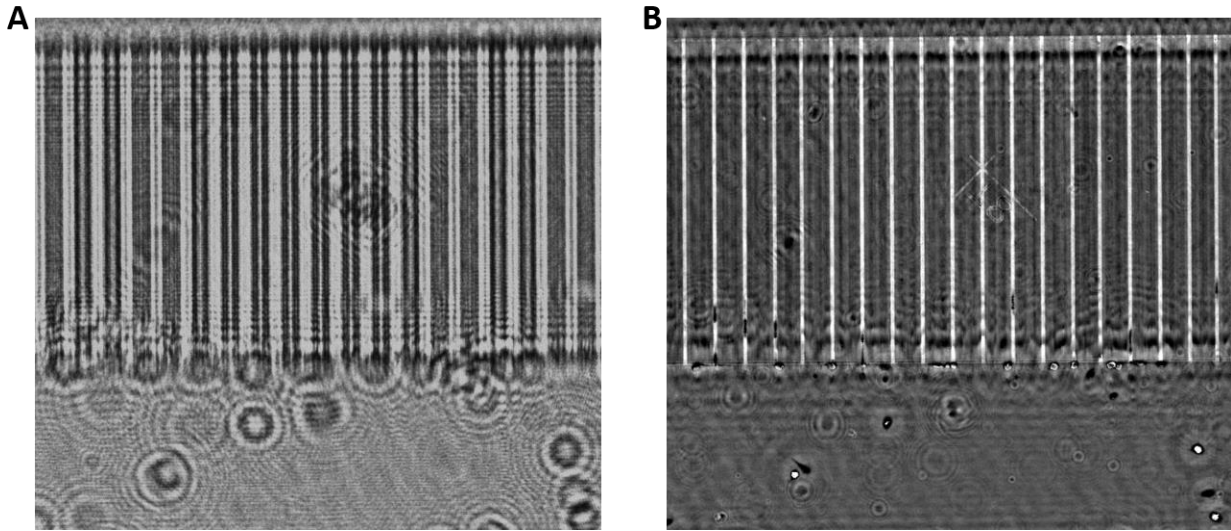


Fig. S1. Reconstruction of a hologram. The LFI recorded hologram (A) is reconstructed to the original object (B) using the Fresnel-Kirchhoff integral. Cells migrating in 6 μm -wide, 10 μm -tall PDMS microchannels are shown.

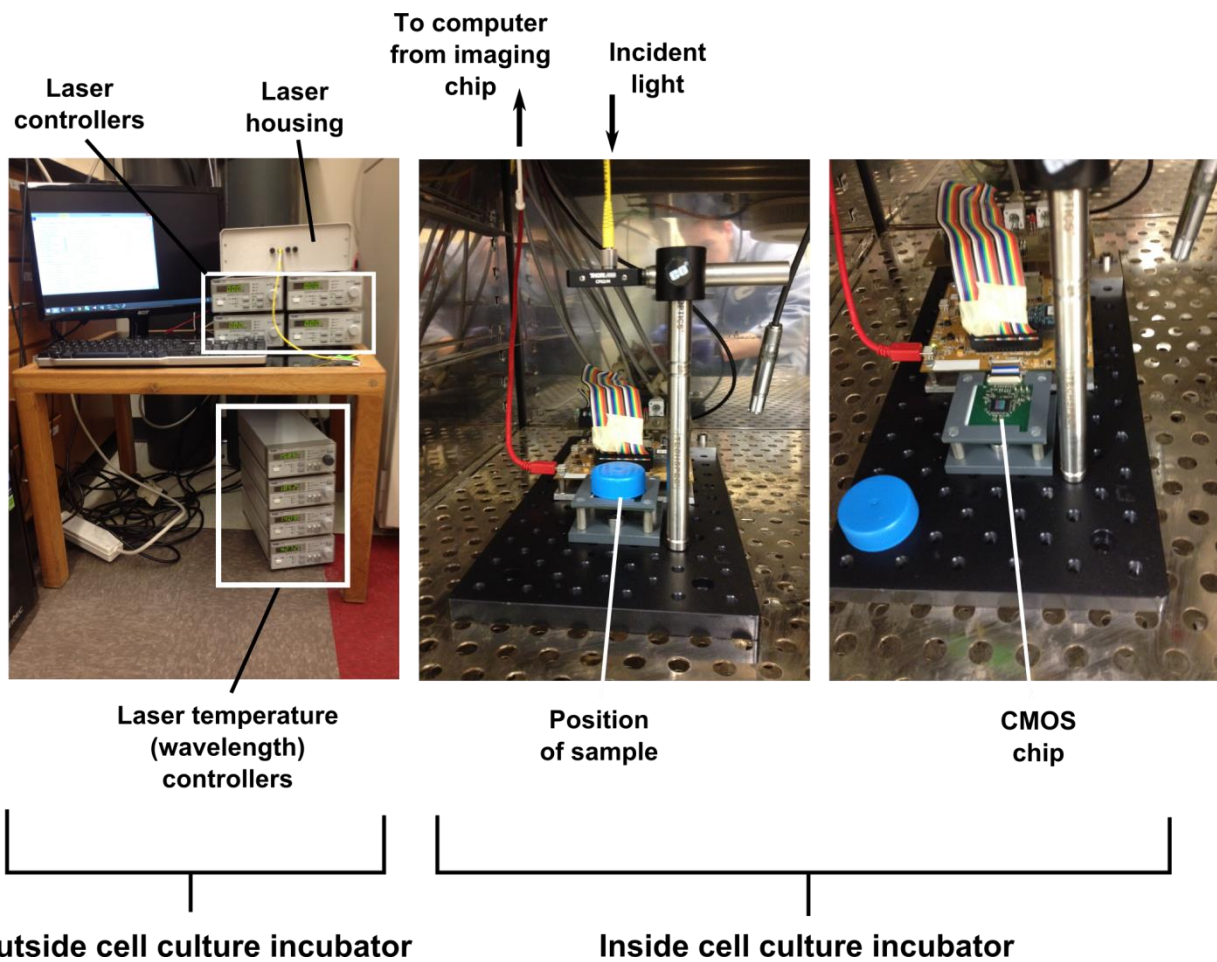


Fig. S2. LFI platform setup. The LFI platform consists of components kept outside and inside of a common cell culture incubator. Programmable laser controllers, laser temperature controllers (which set the wavelength of light used), the lasers (housed in a box), and a computer are set up near an incubator. A fiber optic cable and cables controlling the sensor and transmitting the sensor output to a computer are fed inside the incubator. Incident light from the fiber optic cable is transmitted through the sample, which is placed on a platform over a CMOS chip.

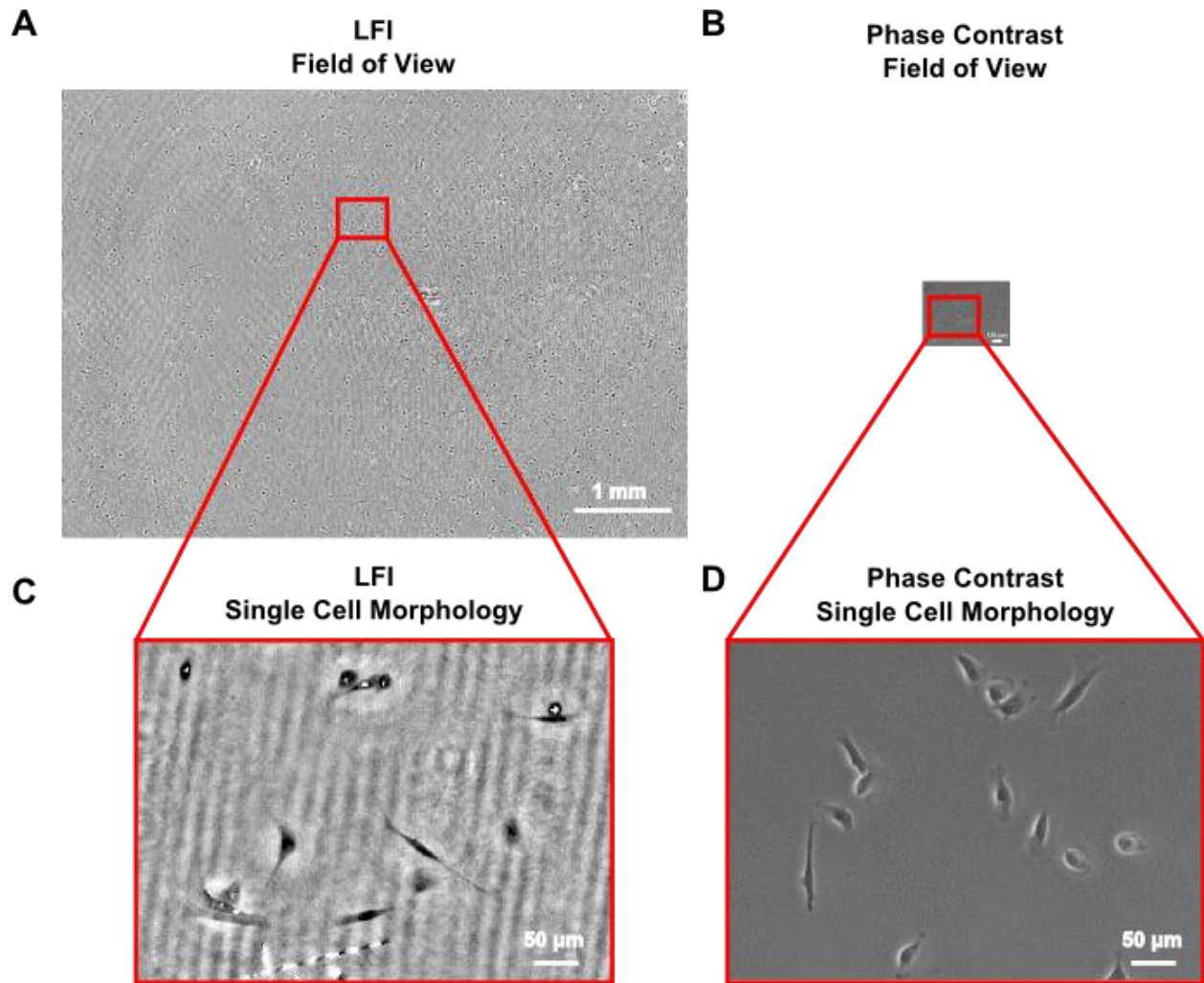
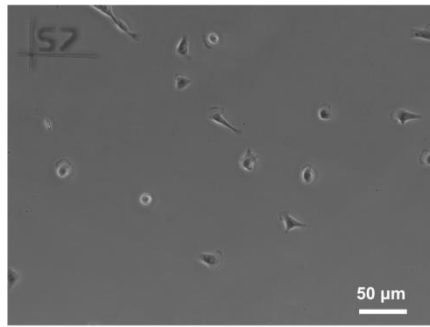
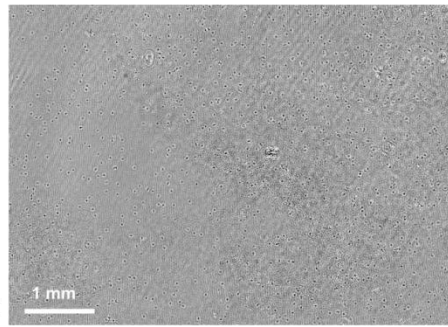


Fig. S3. Comparison of field of view in LFI and phase contrast platforms. (A) Field of view (6.4 mm x 4.6 mm) obtained with a single LFI image. Scale bar represents 1 mm. (B) Field of view obtained with a single phase contrast microscope equipped with a 10x objective. Scale bar represents 100 μm . Morphology of single cells was clearly visible using both (C) LFI and (D) phase contrast microscopy following digital zoom in the images shown in panels (A,B). Images are shown to the same scale. Scale bar represents 50 μm . In (A-D), MDA-MB-231 cells spread on a collagen type I-coated glass slide are shown.

A Random motility assay

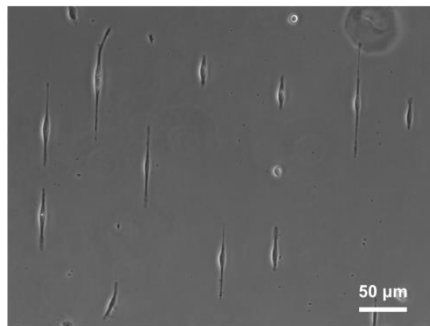


Phase contrast

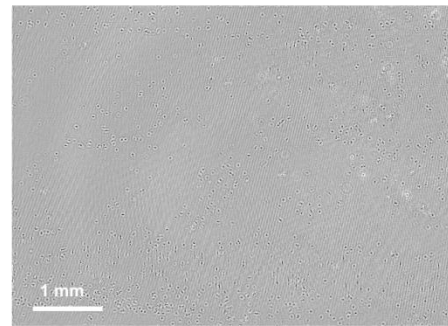


LFI

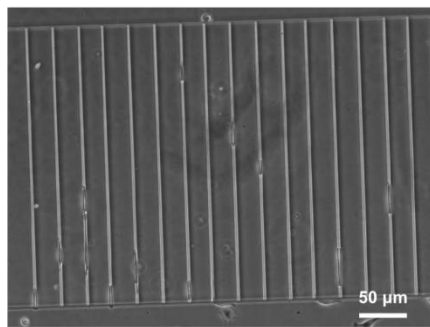
B Microcontact printing migration assay



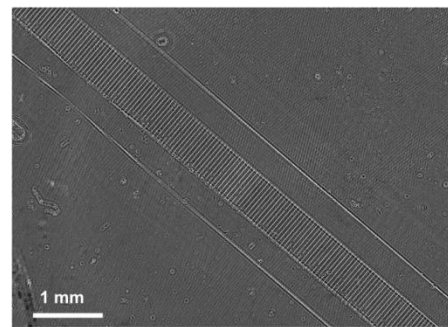
Phase contrast



C Microchannel migration assay



Phase contrast



LFI

Fig. S4. Representative images from the cell migration assays illustrate the large field of view of the LFI platform. Unprocessed, unzoomed images from each assay for the phase contrast (10x, 0.45 NA objective) and LFI imaging platforms are shown. LFI offers a significantly larger field of view for a single image. Assays shown are **(A)** random motility assay, **(B)** microcontact printed line migration assay, and **(C)** microchannel migration assay, all performed with MDA-MB-231 cells. In phase contrast images, scale bar represents 50 μm. In LFI images, scale bar represents 1 mm.

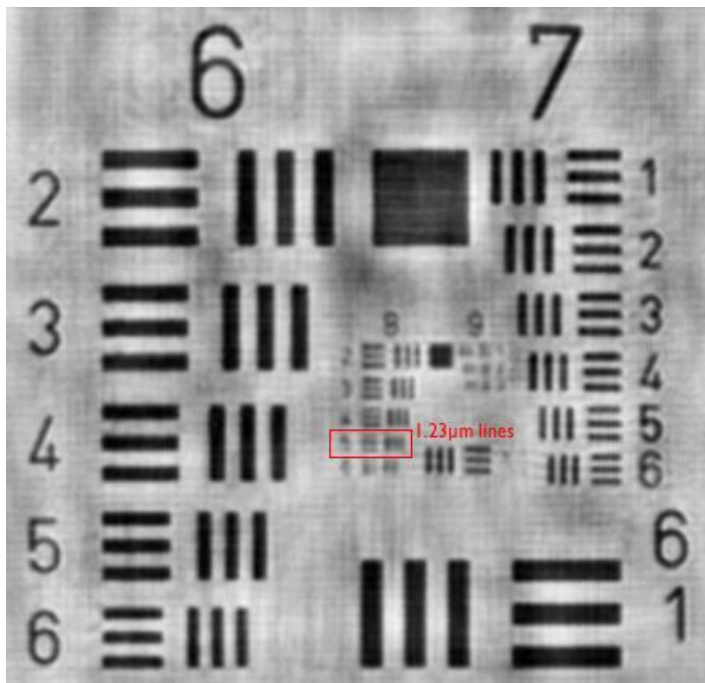


Fig. S5. LFI resolution is determined using US Air Force resolution test chart. To determine the resolution of the LFI set-up the 1951 US Air Force resolution test chart was imaged. This digital zoom demonstrates that the pattern can be resolved up to the 5th element of the 8th group, consisting of 3 microlines with a width of 1.23 μm . The 6th element, consisting of 1.1 μm wide lines, can not be resolved.

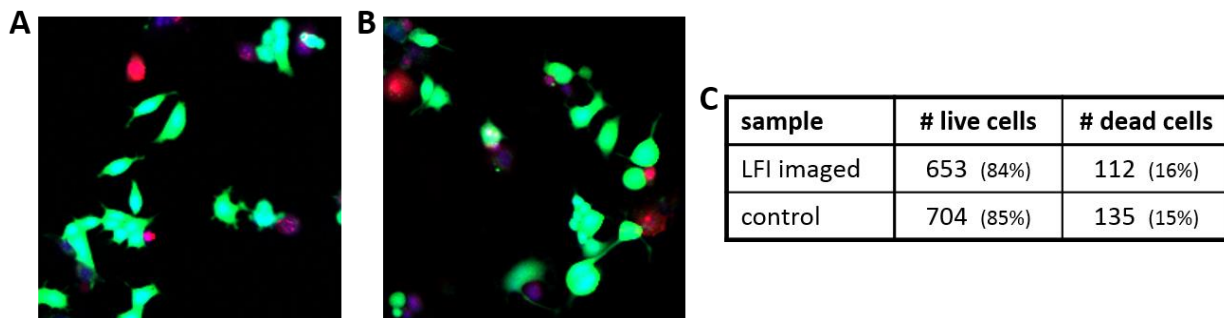


Fig. S6. MCF7 cell viability is not altered by 24 h time-lapse LFI imaging. Cell viability of sparsely seeded MCF7 cells that were imaged using the LFI platform every 10 min for more than 24 h was tested (A) using a cell nucleus stain (Hoechst 33342, blue), a live cell stain (Calcein AM, green), and a stain for dead cells (Propidium Iodide, red). Cells imaged via LFI were compared to a similarly prepared control sample (B) kept in the same incubator but not imaged. Cell counts are summarized in (C).

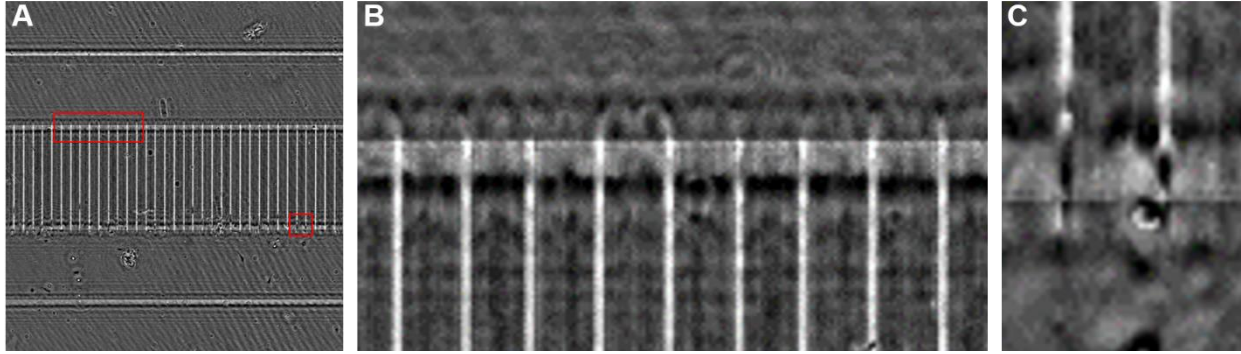


Fig. S7. Laser generated noise. A wave pattern can be observed in those areas of the reconstructed image in which structures are not present, this pattern is due to speckle noise originating from the laser illumination **(A)**. Next to this, edge artifacts and multiple reflection interference are other sources of noise that are present in the lens-free images **(B)**, resulting in dark areas and ring-like patterns around the edges of the microchannels. Also, a pattern of shadow lines in between the consecutive microchannels is generated due to multi-interference. Cells that are located close to the edges of the microchannels can be partially blurred as a result of this interference generated by the microstructures **(C)**.

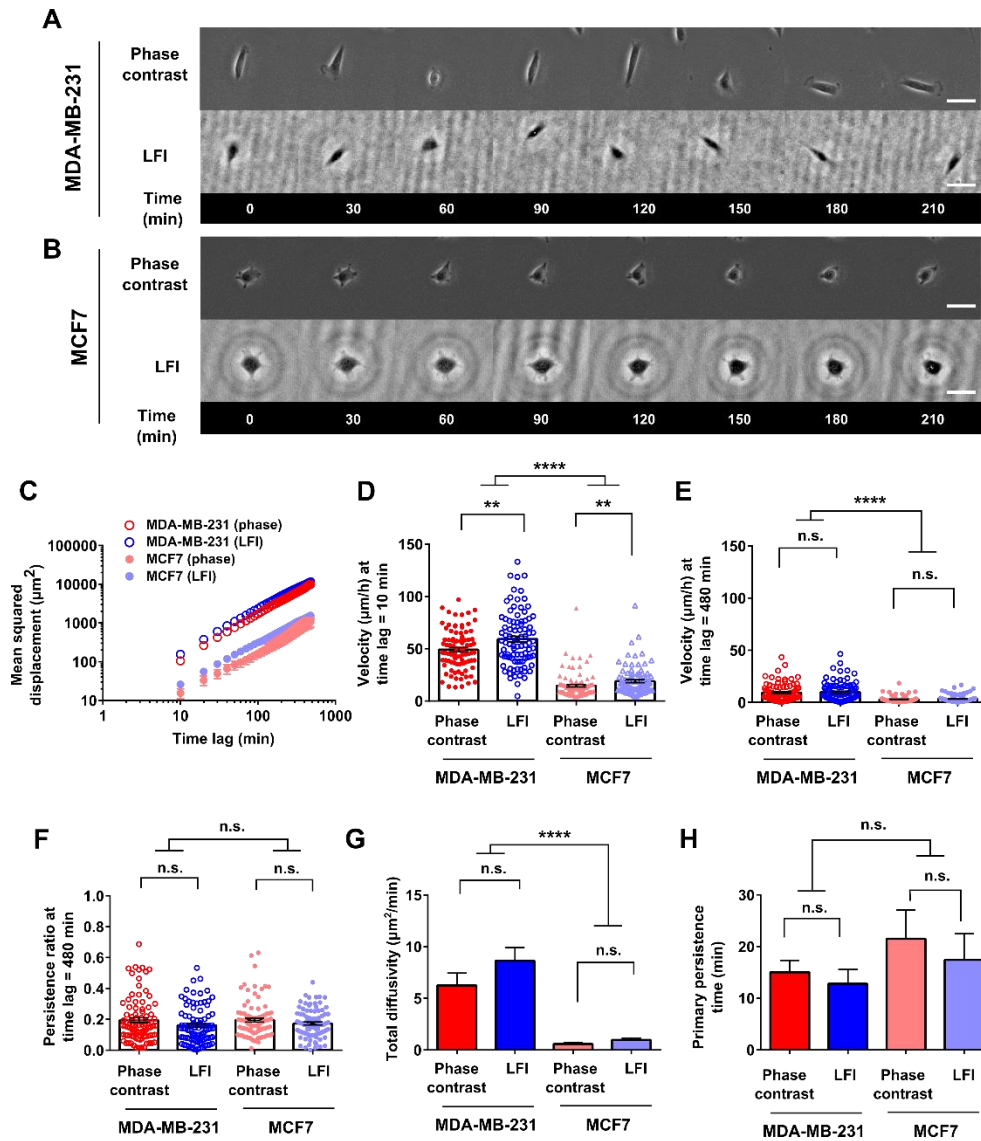
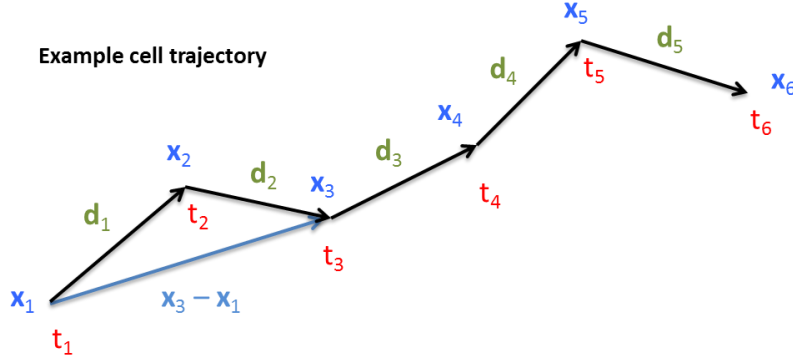


Fig. S8. Phase contrast and LFI imaging platforms generate similar results for random motility assays over longer imaging times (8 h). Time-lapse images of (A) MDA-MB-231 and (B) MCF7 breast adenocarcinoma cells migrating on collagen type I-coated glass slides and imaged using either phase contrast microscopy (10x, 0.45 NA objective) or the LFI platform. Scale bars represent 50 μm . (C) Mean-squared displacements observed for the two cell types with each imaging platform. Velocities for time lags of (D) 10 min and (E) 120 min. (F) Persistence ratio at a time lag of 480 min. (G) Total diffusivity observed for the two cell types with each imaging platform. (H) Primary persistence time observed for the two cell types with each imaging platform. For all metrics, cell trajectories were analyzed over 8 h. $N=90$ cells/condition, with 30 cells/experiment analyzed over 3 independent experiments. Statistical significance between phase contrast and LFI imaging results was analyzed by an unpaired t test if cells passed the D'Agostino and Pearson omnibus normality test, or by Mann-Whitney test if they did not. Differences between MDA-MB-231 and MCF7 cells were assessed by Kruskal-Wallis test with Dunn's multiple comparisons post-test. n.s., difference not statistically significant; **, $p<0.01$; ****, $p<0.0001$.

Example cell trajectory



\bar{x}_i = position vector i

t_i = time i

$\Delta t = t_{i+1} - t_i$

\bar{d}_i = displacement vector $i = \bar{x}_{i+1} - \bar{x}_i$

$\|\bar{d}_i\|$ = length of displacement vector \bar{d}_i

$\text{velocity}(\tau = \Delta t) = \frac{\frac{\ \bar{d}_1\ }{(t_2 - t_1)} + \frac{\ \bar{d}_2\ }{(t_3 - t_2)} + \frac{\ \bar{d}_3\ }{(t_4 - t_3)} + \frac{\ \bar{d}_4\ }{(t_5 - t_4)} + \frac{\ \bar{d}_5\ }{(t_6 - t_5)}}{5}$ $\text{velocity}(\tau = 2\Delta t) = \frac{\frac{\ \bar{x}_3 - \bar{x}_1\ }{(t_3 - t_1)} + \frac{\ \bar{x}_4 - \bar{x}_2\ }{(t_4 - t_2)} + \frac{\ \bar{x}_5 - \bar{x}_3\ }{(t_5 - t_3)} + \frac{\ \bar{x}_6 - \bar{x}_4\ }{(t_6 - t_4)}}{4}$ $\text{velocity}(\tau = 5\Delta t) = \frac{\ \bar{x}_6 - \bar{x}_1\ }{(t_6 - t_1)}$	$\text{MSD}(\tau = \Delta t) = \frac{(\ \bar{d}_1\)^2 + (\ \bar{d}_2\)^2 + (\ \bar{d}_3\)^2 + (\ \bar{d}_4\)^2 + (\ \bar{d}_5\)^2}{5}$ $\text{MSD}(\tau = 2\Delta t) = \frac{(\ \bar{x}_3 - \bar{x}_1\)^2 + (\ \bar{x}_4 - \bar{x}_2\)^2 + (\ \bar{x}_5 - \bar{x}_3\)^2 + (\ \bar{x}_6 - \bar{x}_4\)^2}{4}$ $\text{MSD}(\tau = 5\Delta t) = (\ \bar{x}_6 - \bar{x}_1\)^2$
$\text{persistence}(\tau = \Delta t) = \frac{\frac{\ \bar{x}_2 - \bar{x}_1\ }{\ \bar{d}_1\ } + \frac{\ \bar{x}_3 - \bar{x}_2\ }{\ \bar{d}_2\ } + \frac{\ \bar{x}_4 - \bar{x}_3\ }{\ \bar{d}_3\ } + \frac{\ \bar{x}_5 - \bar{x}_4\ }{\ \bar{d}_4\ } + \frac{\ \bar{x}_6 - \bar{x}_5\ }{\ \bar{d}_5\ }}{5} = 1$ $\text{persistence}(\tau = 2\Delta t) = \frac{\frac{\ \bar{x}_3 - \bar{x}_1\ }{\ \bar{d}_1\ + \ \bar{d}_2\ } + \frac{\ \bar{x}_4 - \bar{x}_2\ }{\ \bar{d}_2\ + \ \bar{d}_3\ } + \frac{\ \bar{x}_5 - \bar{x}_3\ }{\ \bar{d}_3\ + \ \bar{d}_4\ } + \frac{\ \bar{x}_6 - \bar{x}_4\ }{\ \bar{d}_4\ + \ \bar{d}_5\ }}{4}$ $\text{persistence}(\tau = 5\Delta t) = \frac{\ \bar{x}_6 - \bar{x}_1\ }{\ \bar{d}_1\ + \ \bar{d}_2\ + \ \bar{d}_3\ + \ \bar{d}_4\ + \ \bar{d}_5\ }$	

Fig. S9. Velocity, mean squared displacement (MSD), and persistence ratio as descriptors of cell migration. An example cell trajectory containing six position measurements taken at constant time intervals of Δt is shown. Position vectors are denoted as \mathbf{x}_i . Displacement vectors between consecutive positions are denoted as \mathbf{d}_i . The displacement vector between positions 1 and 3, $\mathbf{x}_3 - \mathbf{x}_1$, is also presented. For illustrative purposes, the calculations to compute velocity, MSD, and persistence ratio at time lags of Δt , $2\Delta t$, and $5\Delta t$ are shown. These calculations can be extended for arbitrary cell trajectory lengths and time lags as described in the Materials and Methods.

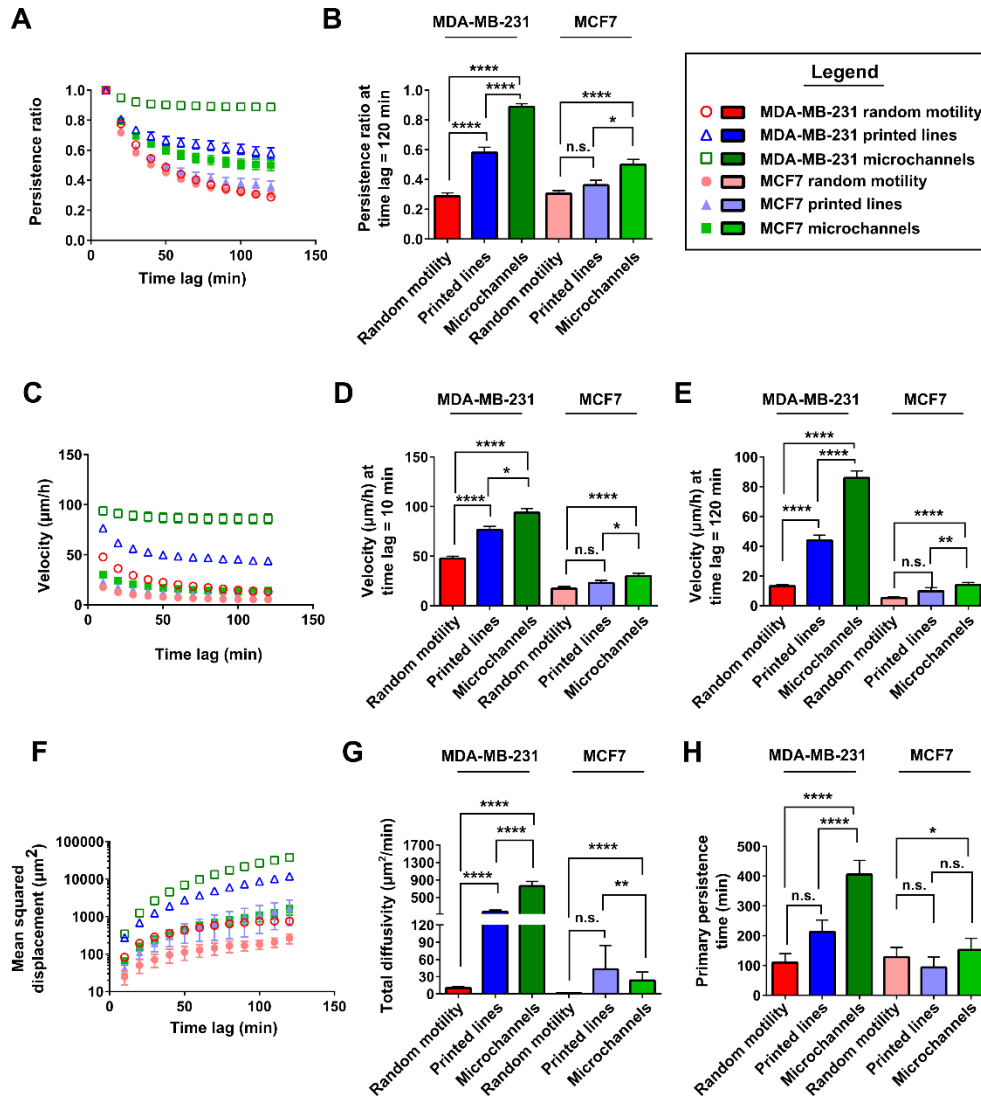


Fig. S10. Increasing confinement results in more efficient cell migration (phase contrast imaging). Data generated via phase contrast imaging across differing levels of physical cell confinement were compared. Persistence ratios were calculated (A) as a function of time lag and (B) at 120 min for both MDA-MB-231 and MCF7 cells in different physical microenvironments. Velocity were determined (C) as a function of time lag and at (D) 10 min and (E) 120 min for both MDA-MB-231 and MCF7 cells in each microenvironment. (F) Mean squared displacement, (G) total diffusivity, and (H) primary persistence time were calculated for MDA-MB-231 and MCF7 cells in each microenvironment. Cells were tracked by phase contrast microscopy for up to 120 min. For MDA-MB-231 cells, N=90 cells/condition, with 30 cells/experiment were analyzed from 3 independent experiments. For MCF7 cells, N=90 cells, with 30 cells/experiment were analyzed from 3 independent experiments from 2D assays; N=60 cells, with 30 cells/experiment were analyzed from 2 independent experiments for printed 1D lines; and N=75 cells, with 25 cells/experiment were analyzed from 3 independent experiments for microchannel results. Comparisons between microenvironments for a given cell type were made with Kruskal-Wallis test with Dunn's multiple comparisons post-test. n.s., difference not statistically significant; **, $p < 0.01$; ***, $p < 0.001$; ****, $p < 0.0001$.

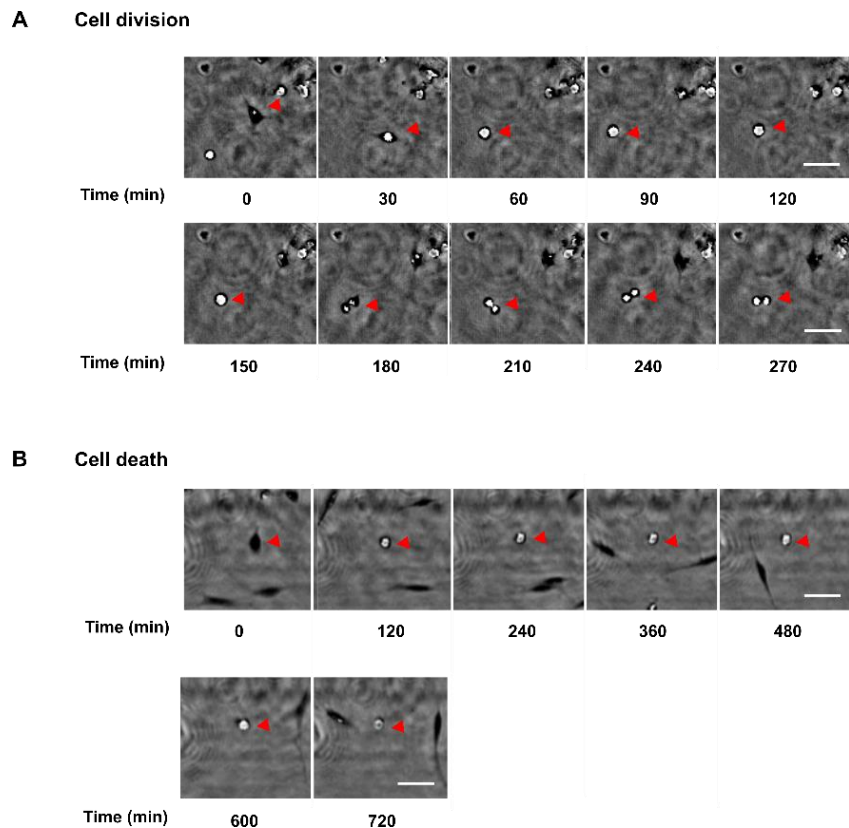


Fig. S11. Lens-free visualization of dividing and dying cells. Time-lapse image sequences showing (A) dividing and (B) dying MDA-MB-231 cells seeded on collagen type I-coated glass substrates. Images were obtained using the LFI setup. Arrows in each panel indicate a given cell followed over time. Scale bar represents 50 μm .

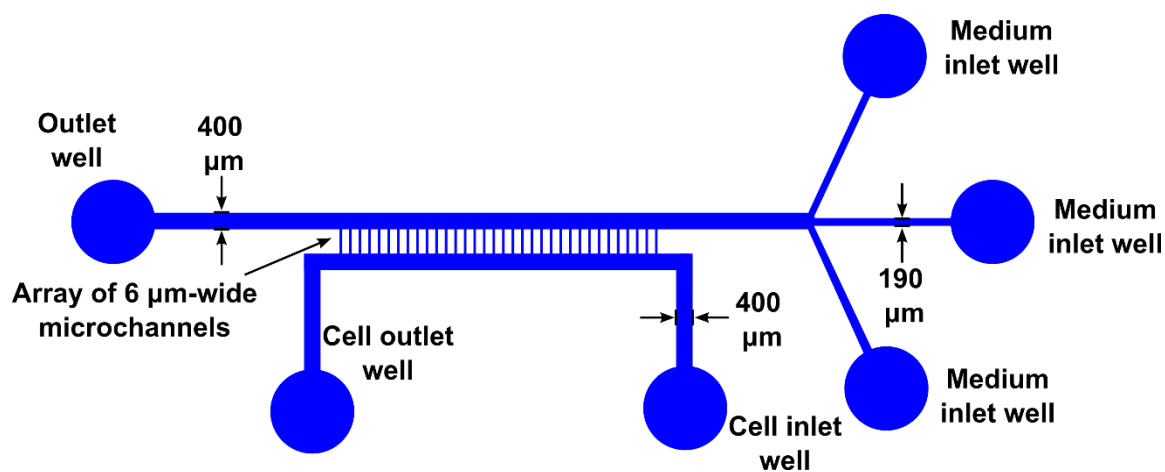
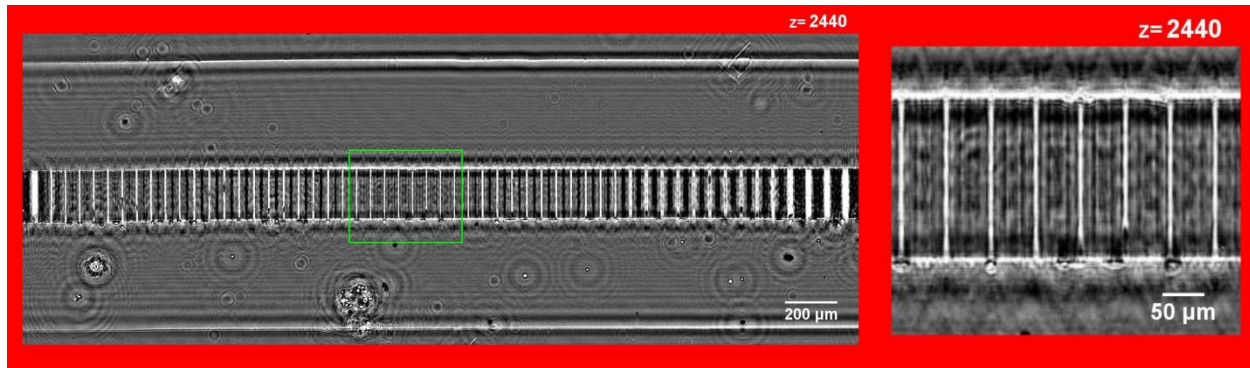
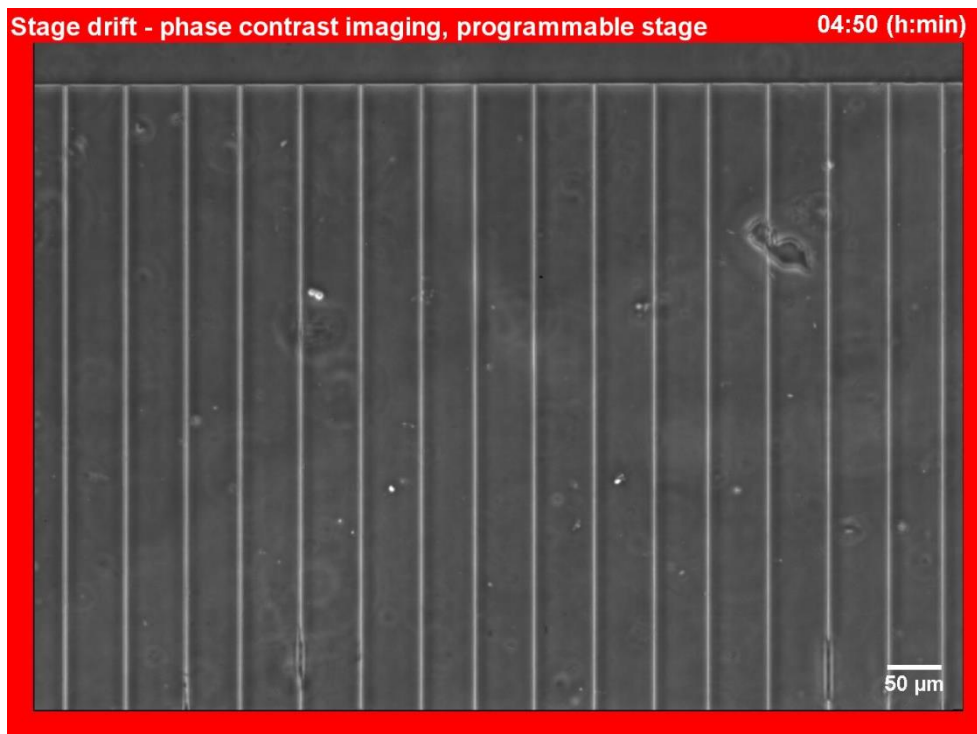


Fig. S12. Microfluidic chip design. Schematic of the microfluidic device used in microchannel migration assays and as a template to print lines for microprinting migration assays. Microchannels ($W=6\ \mu\text{m}$, $L=600\ \mu\text{m}$, $H=10\ \mu\text{m}$) were arrayed perpendicularly to seeding and medium channels ($H=50\ \mu\text{m}$). To seed cells in the device, a cell suspension was added to the cell inlet well, and cells flowed to the microchannel entrances. Following cell seeding, non-adherent cells were washed away, and all six wells of the device were filled with assay medium. Microchannels are not shown to scale.

Supplementary movie legends



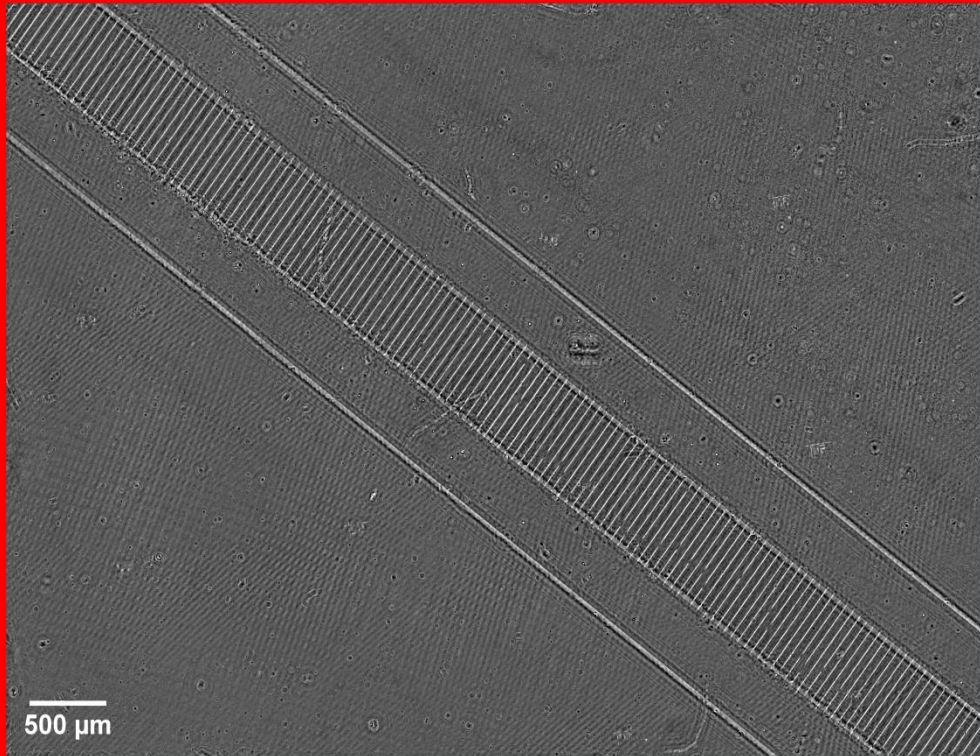
Movies S1. LFI focus is set with a digital parameter. LFI captures all of the information between the light source and the imaging sensor, and the focus (reconstruction plane) is set with a digital parameter. Here, the image reconstruction of a PDMS microchannel device is shown as the object height, z , is varied. The object comes into crisp focus at $z=2430$. The area shown in the inset on the right is indicated by the green box in the left panel.



Movies S2. Stage drift is a common problem in phase contrast live cell imaging. Example of stage drift in phase contrast time lapse imaging. MDA-MB-231 cells migrating through 6 μm-wide, 10 μm-tall PDMS microchannels were imaged every 10 min. The position for image capture was set using a programmable, translating microscope stage and was imaged in series with other positions. The stage “drifted” during the experiment, causing a change in position of the objects and a loss of focus.

Full field of view - LFI

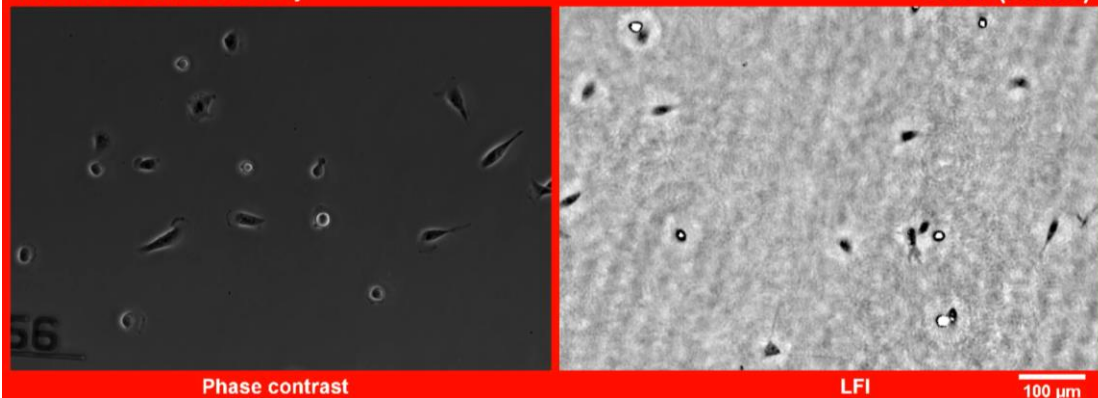
01:30 (h:min)



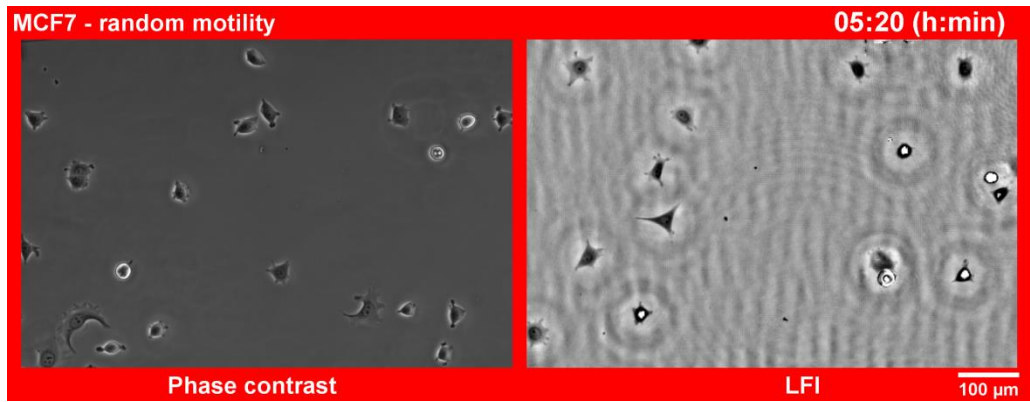
Movies S3. LFI field of view. Full 6.4 mm x 4.6 mm field of view of LFI images. MDA-MB-231 breast adenocarcinoma cells migrating through 6 μm-wide, 10 μm-tall, 600 μm-long PDMS microchannels coated with 20 μg/ml collagen type I were imaged every 10 min. Scale bar represents 500 μm. Cell trajectories over large areas are clearly visible.

MDA-MB-231 - random motility

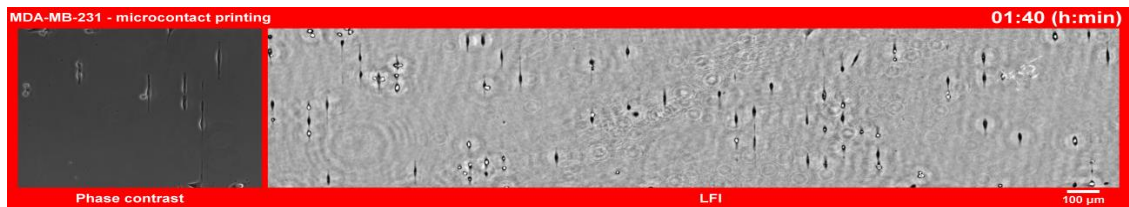
02:10 (h:min)



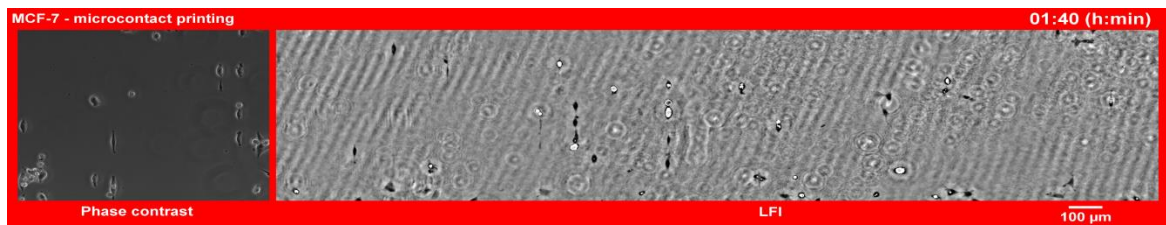
Movies S4. Randomly migrating MDA-MB-231 cells. MDA-MB-231 breast adenocarcinoma cells migrating on a glass slide coated with 20 μg/ml collagen type I were imaged using either phase contrast microscopy or LFI. Images were acquired every 10 min. Cellular position and protrusions were clearly visible in the LFI image. Scale bar represents 100 μm.



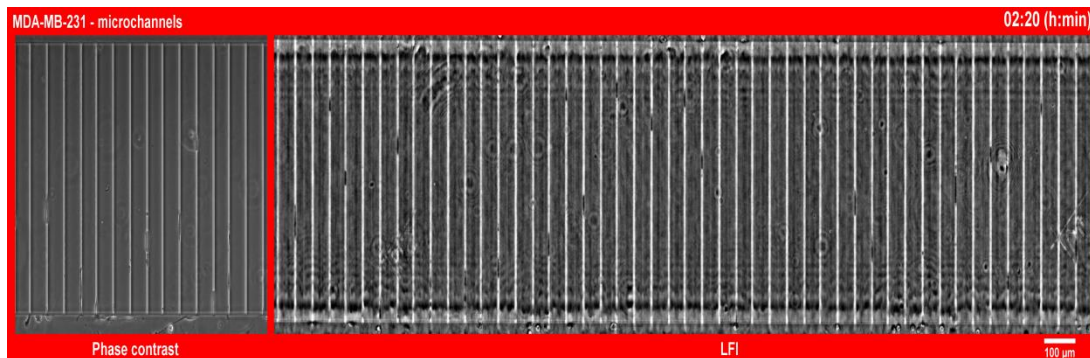
Movies S5. Randomly migrating MCF7 cells. MCF7 breast adenocarcinoma cells migrating on a glass slide coated with 20 µg/ml collagen type I were imaged using either phase contrast microscopy or LFI. Images were acquired every 10 min. Cellular protrusions and, in some cases, nuclear shape were clearly visible in the LFI image. Scale bar represents 100 µm.



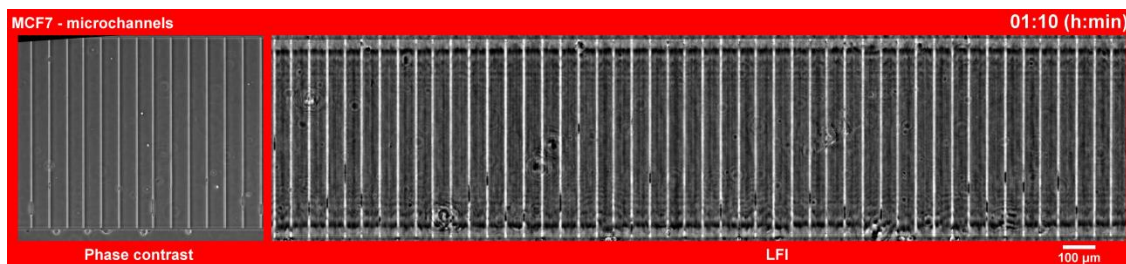
Movies S6. MDA-MB-231 cells migrating on microcontact printed lines. MDA-MB-231 breast adenocarcinoma cells migrating on 6 µm-wide lines of collagen type I (20 µg/ml) were imaged using either phase contrast microscopy or LFI. Images were acquired every 10 min. Cellular position and protrusions were clearly visible in the LFI image. Scale bar represents 100 µm.



Movies S7. MCF7 cells migrating on microcontact printed lines. MCF7 breast adenocarcinoma cells migrating on 6 µm-wide lines of collagen type I (20 µg/ml) were imaged using either phase contrast microscopy or LFI. Images were acquired every 10 min. Cellular position and protrusions were clearly visible in the LFI image. Scale bar represents 100 µm.



Movies S8. MDA-MB-231 cells migrating within microchannels. MDA-MB-231 breast adenocarcinoma cells migrating through 6 μm -wide, 10 μm -tall PDMS microchannels coated with 20 $\mu\text{g}/\text{ml}$ collagen type I were imaged using either phase contrast microscopy or LFI. Images were acquired every 10 min. The position of cells within the microchannels was clearly visible using both imaging techniques. Scale bar represents 100 μm .



Movies S9. MCF7 cells migrating within microchannels. MCF7 breast adenocarcinoma cells migrating through 6 μm -wide, 10 μm -tall PDMS microchannels coated with 20 $\mu\text{g}/\text{ml}$ collagen type I were imaged using either phase contrast microscopy or LFI. Images were acquired every 10 min. The position of cells within the microchannels was clearly visible using both imaging techniques. Note that stage drift in the phase contrast experiment led to loss of focus. Scale bar represents 100 μm .